Dynamics of Rotational Energy Release for Dissociation of Singlet Ketene and the Singlet/Triplet Branching Ratio

Elisabeth A. Wade,[†] Horst Clauberg,[‡] Sang Kyu Kim,[§] Axel Mellinger,[⊥] and C. Bradley Moore*,[||]

Department of Chemistry, University of California, and Chemical Sciences Division, Lawrence Berkeley National Laboratory, Berkeley, California 94720-1460

Received: July 16, 1996; In Final Form: October 10, 1996[⊗]

The rotational energy release in the dissociation of ketene along its singlet potential energy surface is observed and compared with various statistical and dynamical theories. Rotational distributions for $CO(\tilde{X}\ ^1\Sigma^+)(v=1)$ are measured from the threshold for production of $CH_2(\tilde{a}\ ^1A_1)(0,0,0) + CO(\tilde{X}\ ^1\Sigma^+)(v=1)$ to 1720 cm^{-1} above. At low energies ($\leq$200 cm^{-1}), phase space theory (PST) matches the observed distributions. At 357 and 490 cm^{-1}, PST, constrained by the measured state distributions of the methylene fragment, provides a good fit. For $E \geq 1107$ cm^{-1}, the constrained PST matches the average rotational energy observed but gives distributions which are broader than observed. This contrasts with the $^1CH_2$ fragment rotations which become progressively colder than PST as energy increases from 200 cm^{-1} above the threshold. The $CO(v=1)$ rotational distributions for $E \geq 357$ cm^{-1} contain no measurable product from triplet channel fragmentation. They can be compared with the previously determined $CO(v=0)$ rotational distributions in order to partition the yield between singlet and triplet channels and recalculate the singlet yield. This yield is found to be at the upper limit of the range previously reported.

I. Introduction

Statistical rate theories such as Rice−Ramsperger−Kassel−Marcus (RRKM) are providing a qualitatively and quantitatively satisfactory model for the dynamics of unimolecular reactions which pass through a saddle point and therefore a well-defined transition state.[1−4] When there is no barrier for recombination, however, the definition of the transition state and the dynamics of energy flow for a dissociation reaction are much more complex. Several models, including phase space theory (PST),[5] the statistical adiabatic channel model (SACM),[6−8] separate statistical ensembles (SSE),[9] and variational RRKM (var. RRKM),[10−12] have proven to be quantitatively useful for the prediction of rate constants and vibrational excitation of products.[1−4] Models for the dynamics of rotational energy release have very limited predictive value and are often qualitatively unsatisfactory. The first detailed rotational distribution data were for NO from NCNO fragmentation.[13] These data matched the purely statistical distributions of PST from threshold to at least 1800 cm^{-1} above threshold. CO rotational distributions from ketene fragmentation were subsequently fit to a PST distribution for the singlet $[CH_2(\tilde{a}\ ^1A_1) + CO]$ part of the fragmentation yield plus a dynamically controlled Gaussian distribution for the triplet $[CH_2(\tilde{X}\ ^3B_1) + CO]$ part.[14] These results for NCNO and CH_2CO gave a comfortable qualitative and quantitative picture of strong rotation−translation coupling after passage through the transition state and statistical release of energy to product rotations.

Rotational distributions for the photodissociation of HOOH and NO_2 complicated this picture. For NO_2, the NO rotational distributions near the threshold are generally consistent with PST but also exhibit the statistical fluctuations about PST expected when single molecular eigenstates are resolved.[15] However, well above threshold, NO rotational distributions exhibit an oscillatory behavior which is modeled by Franck−Condon overlap of the bending wave functions of a tightened transition state with the free rotor wave functions of NO.[15] For HOOH → 2OH, the rotational distributions produced by exciting overtones of the OH stretch are significantly colder than PST but could be fit by SACM.[16] When a combination band that included the torsional motion as well as the OH stretch was excited, however, the rotational distribution was not statistical, possibly because the initial torsional motion caused additional angular momentum constraints.[16]

Ketene experiments are complicated by its simultaneous fragmentation to both singlet and triplet CH_2.[3] The lowest electronic states of ketene are illustrated in Figure 1. Upon excitation to the S_1 state, the molecule undergoes rapid internal conversion and/or intersystem crossing to the lower electronic states.[3] Measurements on $^1CH_2$ from ketene dissociation give statistical (PST) distributions for rotational excitation from threshold to 200 cm^{-1} above. However, at higher energies the rotational distributions become progressively colder than statistical, reaching a factor of 5 colder at 2900 cm^{-1} above threshold. The $^1CH_2(J_{K_aK_c})$ rotational distributions[17,18] suggest that CO rotational distributions should be reexamined for departures from statistical behavior at energies well above threshold. An approach is suggested by the finding of Kim *et al.* that for $CO(v=1)$ produced at 357 cm^{-1} over its threshold there is no contribution from the triplet channel.[14] Recently, Wodtke and co-workers have also measured correlated-product-state distributions for $CO(v=1; J_{CO}=4,6,8)$ at 308 nm, 208 cm^{-1} above the $CO(v=1)$ production threshold.[19] While some triplet channel contribution was observed, the relative signal due to the triplet channel was much smaller than would be expected for $CO(v=0)$ at the same energy over its threshold. Thus, $CO(v=1,J_{CO})$ distributions are measured as a function of excitation

[†] Current address: Department of Chemistry, San Jose State University, San Jose, CA 95192. E-mail address: ewade@moore3.cchem.berkeley.edu.
[‡] Current address: Eastman Chemical Co., Kingsport, TN 37662. E-mail address: clauberg@tricon.net.
[§] Current address: Department of Chemistry, Inha University, Inchon (402-751), Republic of Korea.
[⊥] E-mail address: axel@moore3.cchem.berkeley.edu.
[||] E-mail address: cbmoore@garnet.berkeley.edu.
[⊗] Abstract published in *Advance ACS Abstracts,* December 15, 1996.

S1089-5639(96)02131-7 CCC: $14.00

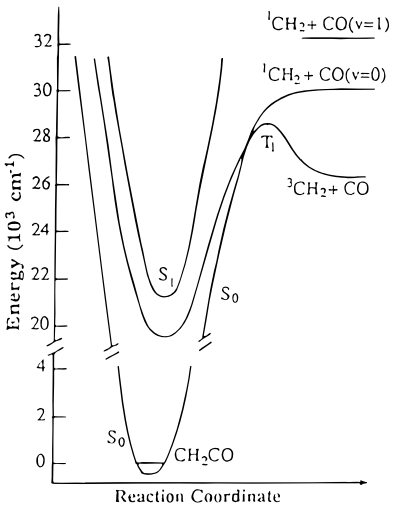

Figure 1. Three lowest potential energy surfaces of ketene along the reaction coordinate. The ketene molecule is excited by a UV laser pulse to the first excited singlet state (S_1), undergoes internal conversion to S_0 and intersystem crossing to T_1, and dissociates into $CH_2(\tilde{a}\ ^1A_1)$ + $CO(\tilde{X}\ ^1\Sigma^+)$ (singlet channel) or $CH_2(\tilde{X}\ ^3B_1)$ + $CO(\tilde{X}\ ^1\Sigma^+)$ (triplet channel) fragments, which have thresholds at 30116.2 ± 0.2 and 28250 ± 10 cm^{-1}, respectively. Also shown is the threshold for the vibrationally excited singlet channel, $CH_2(\tilde{a}\ ^1A_1)$ + $CO(\tilde{X}\ ^1\Sigma^+, v=1)$.

energy in this work in order to determine the dynamics of energy release to CO for dissociation on the singlet surface.

The singlet reaction channel dominates from a few hundred cm^{-1} above its reaction threshold.[14,20] Hayden *et al.* found that the singlet yield at 308 nm, 2351 cm^{-1} above the singlet channel threshold, is at least 0.9.[20] Kim *et al.* calculated the singlet yield assuming that the singlet channel CO rotational distributions are given accurately by PST. Accurate determinations near threshold were possible, but only an estimate of 0.75 ± 0.2 could be derived at 2521 cm^{-1}.[14] Recent measurements of correlated-product-state distributions for CO at 308 nm by Wodtke and co-workers show that the yield is at the upper limit of this range.

II. Experimental Section

Ketene is seeded in helium carrier gas and cooled by supersonic expansion into a vacuum chamber. The cold ketene is photolyzed with a pulse of tunable UV light (288−310 nm), and the CO is excited by a vacuum-UV pulse (141−143 nm). Two CO electronic transitions are used: $\tilde{X}\ ^1\Sigma^+(v=0,J_{CO}) \rightarrow \tilde{A}\ ^1\Pi\ (v'=3,J'_{CO})$ and $\tilde{X}\ ^1\Sigma^+(v=1,J_{CO}) \rightarrow \tilde{A}\ ^1\Pi\ (v'=5,J'_{CO})$. The vacuum-UV fluorescence is detected with a solar blind photomultiplier tube (PMT). The apparatus is generally as described in ref 14, except for the following changes.

For short wavelengths, λ < 300 nm (>1000 cm^{-1} above the $CH_2(\tilde{a}\ ^1A_1)$ ($^1CH_2$) + $CO(v=1)$ threshold), delay times of up to 200 ns between the photolysis and the probe lasers are required, as the solar blind PMT is sensitive to scattered photolysis light. The second harmonic of a Spectra-Physics DCR-4 is used to pump the photolysis laser, Lambda-Physik FL2002 (rhodamine 610 and rhodamine 590). This output is doubled in a KDP crystal to provide the photolysis pulse. A second Nd:YAG, a Quantel YG-682, is used to pump the probe laser, a Spectra-Physics PDL-3 (coumarin 440) whose output is tripled in Xe to provide vacuum-UV.

At energies 200−1000 cm^{-1} above the $^1CH_2$ + $CO(v=1)$ threshold, the solar blind PMT is not sensitive to the photolysis light, λ > 300 nm. A single Spectra-Physics DCR-4 is used to pump both photolysis and probe dye lasers. The second and third harmonics are separated, and the 532 nm is used to pump the photolysis laser (rhodamine 640, sulfarhodamine 640, and Kiton red 620), while the 355 nm is used to pump the probe laser (coumarin 440). This method restricts the delay between pump and probe to <50 ns. For lower energies, the amount of $CO(v=1)$ produced is very small, so the resultant signal-to-noise ratio is poor. Resonant four-wave mixing in Mg vapor is used to increase the amount of vacuum-UV produced and to improve the signal-to-noise by a factor of ∼20. A concentric heat pipe oven with Mg vapor as the nonlinear medium, and Kr as the phase-matching gas was used.[21] This method requires two pump lasers with similar beam profiles. In these experiments, the second and third harmonics of a Spectra-Physics DCR-4 are separated. The 532 nm wavelength is used to pump the photolysis laser, a Spectra-Physics PDL-3 (rhodamine 640). The 355 nm wavelength pumps one of the probe lasers, a Lambda-Physik FL2002 (coumarin 440), which is held fixed at the 431.01 nm wavelength of the two-photon Mg transition. The other probe laser, used to tune the vacuum-UV output, is a Lambda-Physik ScanMate 2E, pumped by the 355 nm output of a Quantel YG-682 Nd:YAG laser.

The spectra collected are converted to rotational distributions, as described in ref 14. The photolysis energy was calibrated using a Tl−Ne optogalvanic tube, which calibrated each energy within 0.5−1 cm^{-1}. The population of each rotational state, $P(v,J_{CO})$, is calculated from the observed intensity, $I(v,J_{CO},J'_{CO})$, using the formula given in Greene and Zare, for the case where rotational alignment is neglected,[22]

$$I(v,J_{CO},J'_{CO}) \propto P(v,J_{CO})\, S(J_{CO},J'_{CO})\, A_0^{(0)}\, B(J_{CO},J'_{CO}) \quad (1)$$

where $S(J_{CO},J'_{CO})$ is given by the Hönl−London factor, $A_0^{(0)}$ is the monopole moment which is equal to unity for photofragmentation, and $B(J_{CO},J'_{CO})$ is the excitation-detection configuration factor given by Greene and Zare for the mutually orthogonal geometry. Alignment is neglected in this analysis because several searches have failed to reveal any alignment effects in methylene[17,25] or in CO[14,19] fragments from ketene dissociation.

III. Results

$CO(v=1)$ rotational state distributions are measured at 57, 110, 200, 357, 490, 1107, 1460, and 1720 cm^{-1} over the threshold for production of $CO(v=1)$ (2200, 2253, 2343, 2500, 2633, 3250, 3603, and 3863 cm^{-1}, respectively, over the threshold for production of $^1CH_2(0,0,0)$ and $CO(v=0)$). These distributions are shown in Figure 2, along with their best fits which will be described more completely in section IV. At 57, 110, and 200 cm^{-1} over the $CO(v=1)$ production threshold, there is a bimodal distribution. The sharp peak at low J is due to the singlet channel, and the broad distribution at higher J is due to the triplet. The fractional yield of $CO(v=1)$ for the singlet channel, assuming that the yield for the singlet and triplet channels totals unity, is measured as 0.4 ± 0.1, 0.5 ± 0.1, and 0.80 ± 0.05 for 57, 110, and 200 cm^{-1}, respectively. At higher energies, there is no measurable triplet channel contribution observed, and the distributions can be assigned purely to the singlet channel.

IV. Modeling Rotational Distributions

These $CO(v=1)$ distributions may be compared to a variety of limiting dynamical models for energy release to the reaction products. The completely statistical limit, in which energy is coupled rapidly among all degrees of freedom as the fragments separate, is PST. In PST, the transition state is assumed to be

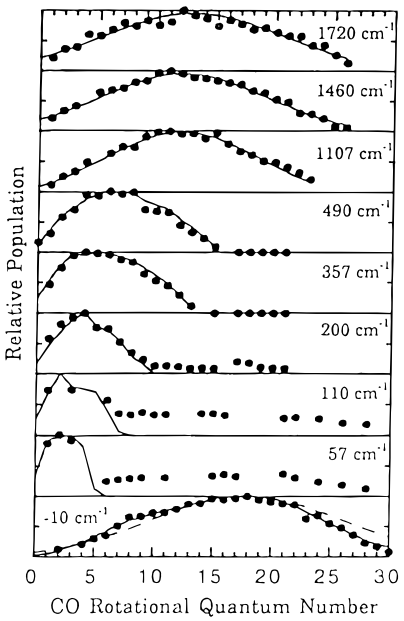

Figure 2. (Bottom distribution, labeled -10 cm^{-1}) CO(v=0) rotational distribution at 10 cm^{-1} below the singlet channel threshold, taken from ref 14. The solid line is the best fit using two Gaussians. The dashed line is the Gaussian centered at $J = 18$ with a width of 11.4 used to fit the CO(v=0) distributions for calculation of the singlet yield. The remaining distributions are rotational distributions of CO(v=1) from ketene dissociation at energy E above the singlet threshold for production of CO(v=1) and fits as described in section IV.

at infinite separation, and the number of open reaction channels at a given energy is simply the total number of accessible states:

$$W(v,J_{CO},J',J'',K_a'',E) = \sum_{J_{K_aK_c}} \sum_{jj=|J_{K_aK_c}-J_{CO}|}^{jj=J_{K_aK_c}+J_{CO}} \sum_{l=|J'-jj|}^{l=J'+jj} \Theta(E + E_{rot.}(J'',K_a'') - D_0 - E_{CO} - E_{CH_2}) \quad (2)$$

where $W(v,J_{CO},J',J'',K_a'',E)$ is the number of accessible states at that energy for a given state of CO, (v,J_{CO}); $J_{K_aK_c}$ denotes the rovibrational states of methylene; E_{CH_2} and E_{CO} are the internal energy of methylene and CO, respectively; v is the vibrational state of CO; J' and J'' are the rotational quantum numbers of excited state and ground state ketene, respectively, such that $J' = J''$ or $J'' \pm 1$; K_a'' is the K_a quantum number for ground state ketene, which is treated as a prolate symmetric top; l is the orbital angular momentum quantum number; $E_{rot.}$ is the initial rotational energy of the parent ketene molecule; D_0 is the threshold energy for singlet dissociation; and $\Theta(x)$ is the Heaviside function. To determine a rotational distribution, $P(v,J_{CO},J',J'',K_a'',E)$ is calculated for each J_{CO} state and averaged over $J' = J'' \pm 1$, J'', and K_a'' for a Boltzmann rotational distribution at 4 K

$$P(v,J_{CO},J',J'',K_a'',E) = W(v,J_{CO},J',J'',K_a'',E) \Big/ \sum_{J'_{CO}} W(v,J'_{CO},J',J'',K_a'',E) \quad (3)$$

$$P(v,J_{CO},E) = \sum_{J',J'',K_a''} P(J',J'',K_a'')\, P(v,J_{CO},J',J'',K_a'',E) \quad (4)$$

where $P(J',J'',K_a'')$ is the product of the Boltzmann rotational distribution for the ground state and the Hönl−London factor for the transition. The resulting distributions are shown in Figures 2−4.

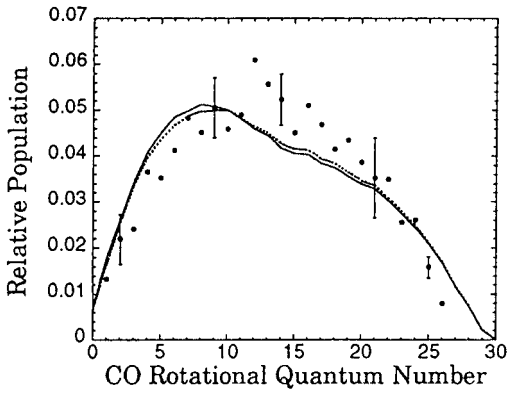

Figure 3. Comparison of two CPST predictions at 1720 cm^{-1} based on different models of the $^1CH_2$ distributions. The closed circles are the experimental points. Sample 1σ error bars are given. The solid line is the resultant distribution when the $^1CH_2$ rotational population is approximated by the Boltzmann distribution which best fits the data.[17] The population is cut to zero for any $^1CH_2$ state whose term value is greater than the available energy. The dotted line is the resultant distribution when that Boltzmann distribution is truncated at 80% of the available energy.

The rotational distribution of methylene has been measured[17] and is known to be significantly colder than PST for energies well above the reaction threshold. Thus, it makes sense to calculate the most random distribution of CO(v=1,J_{CO}) consistent with the observed $^1CH_2$ rotational distribution. The energy available for the CO fragment is assumed to randomize freely subject to the constraint of the observed methylene distributions.[17] In this constrained PST (CPST), a PST distribution for the CO(v=1) fragment is calculated for each energetically accessible $^1CH_2$ rovibrational state.

$$W(v,J_{CO},J_{K_aK_c},J',J'',K_a'',E) = \sum_{jj=|J_{K_aK_c}-J_{CO}|}^{jj=J_{K_aK_c}+J_{CO}} \sum_{l=|J'-jj|}^{l=J'+jj} \Theta(E+E_{rot.}(J'',K_a'') - D_0 - E_{CO} - E_{CH_2}) \quad (5)$$

These distributions are then weighted by the experimental population of that $^1CH_2$ rovibrational state,[17] $P_{exp}(E,J_{K_aK_c})$, and summed together. The $P_{exp}(E,J_{K_aK_c})$ for $^1CH_2$ + CO(v=1) is assumed to be the same as that for $^1CH_2$ + CO(v=0), where E is referenced to the respective product vibronic channel thresholds. Dynamics beyond the transition state appear to be vibronically adiabatic,[3] and there is no reason to expect a substantial difference in rotation−translation couplings and dynamics to result from the small difference in bond length or dipole moment between CO(v=0) and CO(v=1).

$$P(v,J_{CO},J_{K_aK_c},J',J'',K_a'',E) = W(v,J_{CO},J_{K_aK_c},J',J'',K_a'',E) \Big/ \sum_{J'_{CO}} W(v,J'_{CO},J_{K_aK_c},J',J'',K_a'',E) \quad (6)$$

$$P(v,J_{CO},J',J'',K_a'',E) = \sum_{J_{K_aK_c}} P(v,J_{CO},J_{K_aK_c},J',J'',K_a'',E)\, P_{exp}(J_{K_aK_c},E) \quad (7)$$

When the experimental population of $^1CH_2$ matches PST, PST and CPST are identical.

Since the previously measured $^1CH_2$ rotational distributions did not include all accessible rovibrational states,[17] the distributions are approximated by calculating a Boltzmann distribution at the appropriate temperature for the energy of interest, estimated by a linear fit to the Boltzmann temperatures

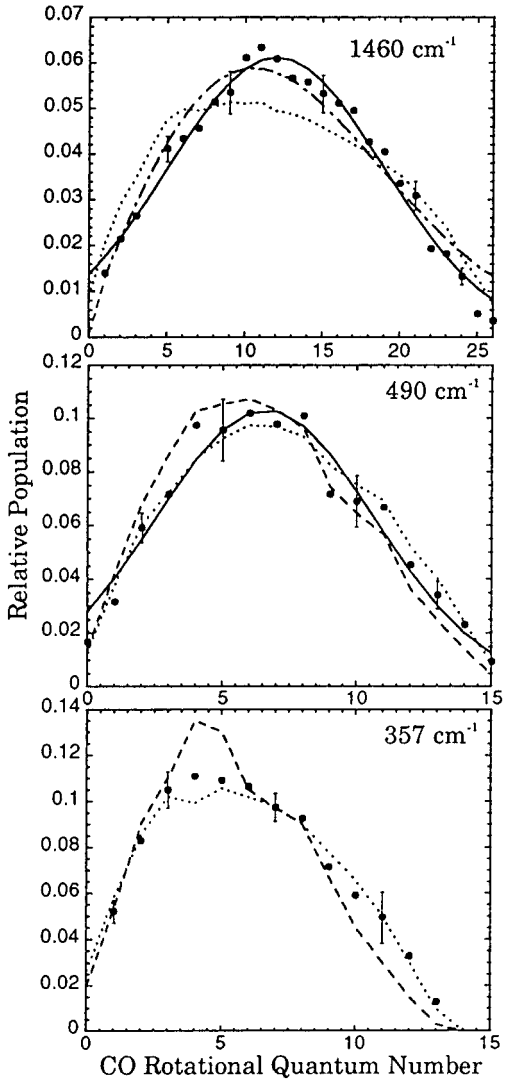

Figure 4. Comparison of experiment, PST, and CPST for CO(v=1) rotational distributions. The solid circles are the experimental points, and the sample error bars are 1σ. The curves are as follows: PST (dashed lines), CPST (dotted lines), Gaussian (solid lines), and Boltzman (dotted-dashed lines).

determined in ref 17. The Boltzmann distributions are cut to zero population at the maximum available energy. It is possible that CPST overestimates low-J_{CO} states in the CO(v=1) rotational distributions (see Figure 4) because $^1CH_2$ distributions are likely to fall more rapidly than the thermal distributions as the maximum energy is approached. CPST calculations with the high-energy tail of the $J_{K_aK_c}$ distributions cutoff at the maximum and at 80% of the maximum energy are shown in Figure 3. The difference between the resulting CO distributions is smaller than the experimental uncertainties in population measurements and not a concern. The yield of vibrationally excited $^1CH_2(0,1,0)$, above its threshold at 1352.5 cm^{-1} was calculated using SSE,[9]

$$P(v) = \frac{(E - E_v)^{3/2}}{\sum_{v'}(E - E_{v'})^{3/2}} \qquad (8)$$

This expression fits the measured branching ratios.[14,18,24] $P_{exp}(E,J_{K_aK_c})$ for $^1CH_2(0,1,0)$ is approximated by a Boltzmann rotational distribution with $T_{rot.}(E,^1CH_2(0,1,0)) = T_{rot.}(E - (1352.5\ cm^{-1}), ^1CH_2\ (0,0,0))$.[18] The total $P_{exp}(E,J_{K_aK_c})$ for eq 7 is the sum of the Boltzmann rotational distribution for each vibrational state weighted by its vibrational yield. Like PST, CPST contains no adjustable fitting parameters. Calculated distributions are compared to experiment in Figures 2−4.

TABLE 1: Rotational "Temperatures"

E_{exc}[a] (cm^{-1})	$T_{rot.}(K)$ exp	$T_{rot.}(K)$ PST	$T_{rot.}(K)$ CPST	$\bar{E}_{rot.}/E_{exc}$ (%) exp	$\bar{E}_{rot.}/E_{exc}$ (%) CPST
57	34 ± 6	41	41	32 ± 3	31.7
200	88 ± 9	83	83	27 ± 2	27.1
357	167 ± 17	135	162	26.0 ± 0.7	27.0
490	227 ± 23	198	224	26.0 ± 0.7	27.0
1107	602 ± 60	407	*b*	26.0 ± 0.7	26.8
1460	730 ± 73	521	*b*	26.6 ± 0.7	26.2
1720	817 ± 82	589	*b*	25.9 ± 0.9	25.0

[a] E_{exc} is excess energy, $E - D_0$. [b] At these energies, CPST cannot be fit to a Boltzmann plot. See Figure 5.

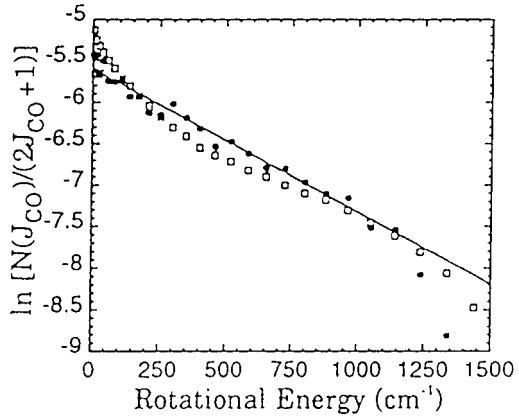

Figure 5. Boltzmann plots at 1460 cm^{-1}. The solid circles are the experimental distribution and the open squares are the CPST distribution. The solid line is the Boltzmann fit to the experimental distribution. While the downward curve at high energy is typical of a PST-like distribution, which does not continue out to infinite energy, the initial curve is not. For the CPST, this initial curve makes it impossible to determine a meaningful slope and temperature.

Neither PST nor CPST adequately describes all of the distributions. PST fits the lowest energy distributions, at 57, 110, and 200 cm^{-1} in Figure 2, just as it describes the $^1CH_2$ distributions and PHOFEX spectra for $E \leq 200$ cm^{-1}.[17] At 357 and 490 cm^{-1}, CPST gives a significantly better fit than PST, Figure 4. For $E \geq 1107$ cm^{-1}, PST overestimates the population of the low-J_{CO} states and underestimates the population of higher J_{CO} states, and CPST matches the center and overestimates the width of the distributions. Several functional forms for the CO(v=1) rotational distributions were tested for $E \geq 490$ cm^{-1}. The best fits were provided by Gaussian (two fitting parameters) and Boltzmann (one fitting parameter) distributions, Figure 4. In Figure 2, the solid lines are given by PST at 57, 110, and 200 cm^{-1}, by CPST at 357 and 490 cm^{-1}, and by the best Gaussian fit at 1107, 1460, and 1720 cm^{-1}. The best fit Boltzmann rotational temperatures are given in Table 1 along with temperatures derived for the PST and CPST distributions. These temperatures are simply fitting parameters and have no fundamental significance as the distributions are not thermal; in fact, for CPST at energies above 1000 cm^{-1} a rotational temperature completely misrepresents the distribution, Figure 5. Table 1 also compares the average fraction of the total available energy released as CO rotation for these different distributions. The measured value is 26 ± 1% for the entire range $1720 \geq E \geq 357$ cm^{-1}.

Doppler-resolved spectra of $^1CH_2$ fragments give the translational energy release distribution. The CO rovibrational

distribution paired to an individual $^1CH_2$ state is then derived by energy conservation. Chang *et al.* report measurements on the 4_{14} rotational level for photodissociation of room temperature ketene at 308 nm, or 2351 cm^{-1} over the singlet channel threshold.[25] They were able to fit these Doppler profiles by assuming that the rotational distribution of CO follows PST, or equivalently CPST since only a single rotational state of $^1CH_2$ is considered, with a population of CO(v=1) twice the average given by SSE.[25] Measurements of the vibrational branching ratio summed over all product rotational states give values identical to those from SSE.[14,18,24] However, the $^1CH_2$ fragments coincident with CO(v=1) are in relatively low-J states compared to those for CO(v=0). Near 308 nm, direct measurements of populations indicate that the rotational distributions of CO, described here, and $^1CH_2$[17,18] are far from PST. Furthermore, CO time-of-flight data, Figures 6−8 of ref 19, suggest that for low $^1CH_2$ rotational energies the J_{CO} distribution is skewed to values much higher than those for PST. The consequence is smaller velocities than those for PST. It might also be possible that some of the fast moving $^1CH_2$ product collides and is thermalized during the 100 ns observation time. The reported fits do not seem to be sufficiently sensitive to the J_{CO} distribution to distiguish between PST and the distributions reported here.

PST calculations may be carried out by including a variety of dynamical constraints. One approach is to restrict the range of impact parameters, b. This in turn limits the orbital angular momentum quantum number l for a given kinetic energy release, E_{trans},

$$b = ((l(l+1)h^2)/2\mu E_{trans})^{1/2} \tag{9}$$

Garcia-Moreno *et al.* found that methylene rotational distributions could be fit better by setting a maximum impact parameter, b_{max}, constrained to a fraction of an angstrom.[17] However, the PHOFEX spectra for such impact parameter constraints were displaced to higher energy from PST and completely inconsistent with experiment.[17,26] This method has recently been used by Wodtke and co-workers, who refer to it as RPST, to fit their correlated product state distributions.[19] For $5 < J_{CO} < 20$, most of the distribution, their data require $b_{max} - b_{min} \sim 0.3$ Å with b_{max} increasing from 0.6 to 1.2 Å as J_{CO} increases from 5 to 20 for $^1CH_2(0,0,0)$ + CO(v=0).[19] These impact parameter ranges are not only inconsistent with PHOFEX data but are also unrealistically small compared to the 2.2−3.1 Å range for the C−C bond length for the variational transition state.[23] The data on rate constant, $^1CH_2$ rotational distributions, and CO time of flight show that the photodissociation of ketene is clearly dynamically constrained. However, a simple limitation on the range of impact parameters does not describe that constraint.

SACM is a statistical model based on a physically different set of dynamical constraints. SACM, like variational RRKM, considers the increase in energy level spacing which occurs as the chemical bond forms betwen the approaching fragments.[23] In SACM, adiabatic channel curves are defined by connecting the transition state energy levels smoothly and without crossings to the asymptotic levels of the freely rotating products.[6−8] The reaction rate is defined by the number of channels with energy maxima less than the total available energy. If the dynamics beyond the maxima were strictly adiabatic repulsion for each channel, only the lowest energy product channels would be observed and each channel would open at an energy well above its asymptotic threshold. Such is not the case for CO or for $^1CH_2$[17,18,24] and indicates that the dissociation dynamics of ketene from transition state to products are clearly not in this strict adiabatic limit. Nevertheless, SACM suggests that repulsive energy release may play a significant role in the dynamics.

The simplest impulsive model predicts that the rotational distribution should be a Gaussian centered around an average rotational energy

$$\bar{E}_{rot.}(CO) = \frac{m_O}{m_C + m_O}(\sin^2\delta)\frac{E_{avl}}{2} \tag{10}$$

where m_O and m_C are the masses of O and C, respectively, E_{avl} is the energy available for rotation of CO and translation, and δ is the angle of the CCO bend at the transition state and beyond.[28] If the bending angle is not a strong function of the excess energy, then the average rotational energy is a constant fraction of the available energy. At 1460 cm^{-1}, 26% of the available energy is converted into CO rotation. This corresponds to $\delta \sim 110°$ if no energy is reserved for $^1CH_2$ rotation. Recent *ab initio* calculations predict the CCO angle at the transition state for the singlet channel to be nearly linear, ∼170°.[23] Allowing for the energy in rotational excitation of $^1CH_2$, impulsive models clearly predict rotational excitation of CO much lower than that observed.

Even at energies over a few hundred cm^{-1}, where the transition state has tightened, the observed CO roational distribution is not so far from the CPST statistical limit and is dramatically different from the adiabatic limit. The basic dynamics of the SACM may be correct if hops through some narrowly avoided crossings are permitted. Such hopping will tend to preserve the rovibrational wave function of the molecule as it proceeds from transition state to products. Thus, a Franck−Condon model might be appropriate. This limiting model is at the opposite extreme from PST which assumes strong coupling among rotational and translational degrees of freedom beyond the transition state. In this limit, the rotational distribution is given by the overlap integral between the bound and free wave functions.[28,29]

$$P(J_{CO}) = |\langle\Psi_{bound}|\Psi_{free}\rangle|^2 \tag{11}$$

where J_{CO} is the rotational quantum number of the product species. This method has been used successfully to calculate rotational distributions by Houston and co-workers for HCO[30] and by Reisler and co-workers for NO_2.[29] For a triatomic, the bending and stretching vibrations of the parent are assumed to be uncoupled, and the free wave functions are given by the spherical harmonics. If parent rotation is not considered and the bending vibration is approximated as a harmonic oscillator,[28]

$$P_n(J_{CO}) \propto \sin^2[(J_{CO}+{}^1/_2)\delta + (-1)^n(\pi/4)] \times H_n^2[\alpha'(J_{CO}+{}^1/_2)]\exp[-(\alpha')^2(J_{CO}+{}^1/_2)^2] \tag{12}$$

where n is the number of quanta in the bending mode, $H_n[x]$ are the Hermite polynomials, δ is the equilibrium bend angle, and α' is a function of the molecular geometry and the bending frequency.[28,29] This model has been applied to ketene, treating CH_2 as an atom and considering only the CCO bend at the transition state, taken from a recent *ab initio* analysis by Klippenstein, et al.[23] The distributions were averaged over the possible vibrational states of the bending vibration at the transition state, using the variational RRKM sum of states for the $3N - 7$ modes at the transition state of ref 23. Since the CCO angle is close to 180°, those vibrational distributions were calculated in two ways, treating the CCO bend as a degenerate or nondegenerate bend. When the bend was assumed to be degenerate, the population at that vibration was multiplied by

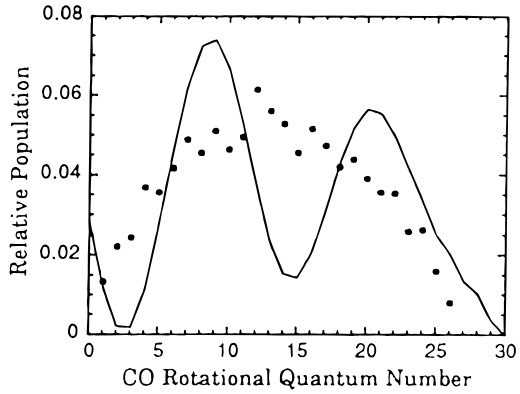

Figure 6. Comparison of experiment and Franck−Condon mapping at 1720 cm^{-1} above the singlet threshold for production of CO(v=1). The solid circles are the experimental points, and the solid line is the distribution produced by Franck−Condon mapping.

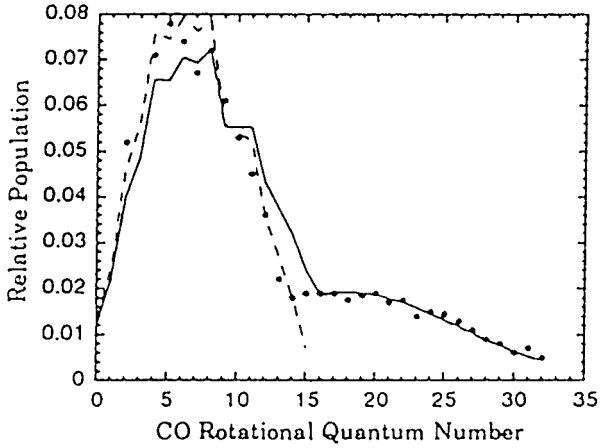

Figure 7. CO(v=0) and CO(v=1) rotational distributions, at 425 and 490 cm^{-1} over the respective thresholds, used to calculate the upper and lower limits on the singlet yield. The solid circles are the CO-(v=0) experimental distribution. The dashed line is the upper limit, given by the CO(v=1) distribution times a scaling factor of 0.78. The solid line is the lower limit, which is the weighted sum of the CO-(v=1) distribution and a Gaussian centered at J = 18 with a width of 11.4 which is used to approximate the CO from the triplet channel. This gives a singlet yield of 0.63.

the degeneracy factor of $n + 1$ and both degenerate bends are considered. Since these assumptions only affected the weighting of the vibrations and not the overall shape of each vibration's rotational distribution, the two distributions were quite similar. The results of this calculation, assuming a nondegenerate bend, are compared with experiment in Figure 6. This model predicts large oscillations in population with J_{CO} such as those that have been observed in HCO[30] and NO_2[29] but are not present in ketene distributions. Inclusion of the $^1CH_2$ degrees of freedom, averaging over initial ketene states, and other refinements will reduce or possibly even eliminate these oscillations. The smoothed result is qualitatively similar to the data.

The release of energy to rotation in singlet channel ketene fragmentation is completely statistical for energies up to 200 cm^{-1} above threshold. As energy increases above 200 cm^{-1}, $^1CH_2$ departs from the strongly coupled limit and receives progressively less than its statistical share of energy as total energy increases. CO continues to be statistically distributed among its rotational states to energies 500 cm^{-1} and possibly approaching 1000 cm^{-1} above threshold. That CO should remain statistical to higher energies than $^1CH_2$ may be understood in terms of the smaller energy level spacings for CO and the consequently smaller rotation−translation couplings required for energy randomization. Above this energy, the average rotational energy and average J_{CO} are still predicted correctly by CPST, Table 1, but the distributions are narrower than statistical. Hence, the dynamics for CO are close to the strongly coupled statistical limit but modestly constrained to populate a narrower range of quantum states while the dynamics for $^1CH_2$ are far from statistical. None of the simple dynamical models discussed to date provide a satisfactory quantitative picture of the dynamics from threshold to a few thousand cm^{-1} above threshold.

V. Singlet Yield

As the CO(v=1) rotational distributions for excess energies ≥357 cm^{-1} contain no discernible contribution from the triplet channel, they can be used to partition the previously determined CO(v=0) rotational distributions[14] into singlet and triplet contributions. Below 200 cm^{-1}, where PST adequately models both the CO(v=0) and the CO(v=1) rotational distributions, the singlet yield is calculated accurately by Kim *et al.*[14] The singlet part of the distribution is modeled by PST, while the triplet part is approximated by a single Gaussian. Above 200 cm^{-1}, the experimental CO(v=1) distributions are assumed, in the present calculation, to be identical to the singlet part of the CO(v=0) distributions taken from ref 14. The singlet yield is calculated in two ways, neither of which perfectly fits the ground state rotational distributions.

First, the singlet yield was calculated by matching the height of the CO(v=1) distribution to the peak of the singlet part of the CO(v=0) distribution. This gives an upper limit, since the contribution of the triplet channel to the population of the J_{CO} at the peak of the singlet channel distribution is ignored. To try to incorporate this contribution, the triplet was modeled, as by Kim *et al.*,[14] as a single Gaussian centered at J_{CO} = 18 with a width of 11.4. This model describes the high-J_{CO} populations, which are completely due to the triplet, but overestimates the triplet where it overlaps the singlet. This approach thus gives a lower limit for the singlet yield. An example of these estimates is given in Figure 7. It was not possible to fit the CO(v=0) rotational distribution perfectly by varying the singlet−triplet branching ratio. This is probably because the triplet rotational distribution is not really a single Gaussian, Figure 2. However, there is no solid basis for choosing a more complex form at the energies considered here. At 1107 cm^{-1}, it was necessary to incorporate another Gaussian, centered at J_{CO} = 7 with a width of 10, in order to account for low-J_{CO} population due to CO associated with vibrationally excited $^3CH_2$. From 357 to 1107 cm^{-1}, the upper and lower limits differ by no more than 0.1, except at 490 cm^{-1}, where they differ by 0.15. This large difference is due to the difference in energy over threshold, 425 and 490 cm^{-1}, at which the CO(v=0) and CO(v=1) distributions, respectively, were measured. While the CO(v=1) distributions were not all collected at exactly the same energies as the CO(v=0) distributions, the energy difference was typically no more than 10%. (See Table 2).

At 1460 and 1720 cm^{-1}, there is no clear difference between the observed CO(v=0) and CO(v=1) rotational distributions (see Figure 8), so a singlet yield of unity is consistent with the data. While some high-J_{CO} points are observed in CO(v=0) that were not detected for CO(v=1), if it is assumed that these high-J_{CO} states contain all of the triplet population at that energy, the resultant triplet yield is so low that the corresponding triplet rate constant decreases with increasing energy, which seems unlikely. Thus, for higher energies, two limiting models are used to extrapolate the triplet rate constant to 6000 cm^{-1} (see Figure 9) and calculate the singlet yields implied.

TABLE 2: Singlet Yields

	singlet yield		
E_{exc}[a](cm^{-1})	ref 14 [b]	lower	upper
57 (56)[c]	0.15 ± 0.03	0.12	0.18
110 (110)[c]	0.34 ± 0.03	0.31	0.37
357 (325)	0.60 ± 0.06	0.60	0.67
490 (425)	0.62 ± 0.06	0.63	0.78
1107 (1107)	0.65 ± 0.10	0.75	0.85
1435	0.70 ± 0.08	0.85	0.88
1720	0.80 ± 0.10	0.86	0.90
2521	0.75 ± 0.20	0.88	0.95
2942		0.88	0.96
3217		0.87	0.97
3538		0.88	0.97
3763		0.85	0.97
4367		0.89	0.99
4870		0.88	0.99
4920		0.88	0.99
5598		0.85	0.99

[a] The values in parentheses are the excess energy (E_{exc})for the CO(v=0) distribution taken from ref 14, while the other value is for the CO(v=1) distribution. Above 1107 cm^{-1}, the singlet yield is approximated from the total rate constants given in ref 31 and the extrapolated triplet rate constants (Figure 9); the energy is that at which the total rate constant was measured. [b] No singlet yield was calculated above 2500 cm^{-1}. [c] At 57 and 110 cm^{-1}, the distribution is described by PST, so the yield is calculated as in ref 14.

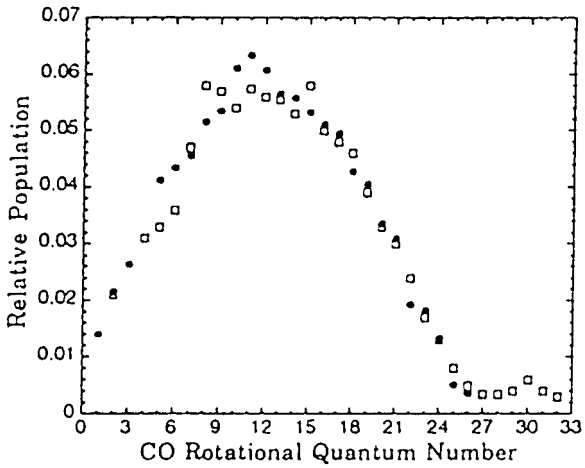

Figure 8. CO(v=0) and CO(v=1) rotational distributions, at 1435 and 1460 cm^{-1} over the respective thresholds. The open squares are the CO(v=0) distribution, and the solid circles are the CO(v=1) distribution. There is essentially no difference between the distributions.

In the lower limit case, the triplet rate constant is assumed to be constant above 1107 cm^{-1}, so that

$$k_t(E>1107) = k_t(1107) \tag{13}$$

Since the total rate constants in this energy region have been determined by Zewail and co-workers,[31] this approximated triplet rate constant allows for the calculation of a singlet rate constant,

$$k_s(E>1107) = k_{tot.}(E>1107) - k_t(1107) \tag{14}$$

As this method underestimates the triplet and so overestimates the singlet, another method was used to give a lower limit for the singlet yield.

The upper limit for k_t was calculated by extrapolating from the known triplet rate constants. The triplet rate constants below the singlet threshold have been determined by Chen *et al.*[32] Additionally, triplet rate constants were calculated from the total rate constants[31] and the experimental singlet yields at 490 and 1107 cm^{-1} (450 and 1107 cm^{-1} in ref 31),

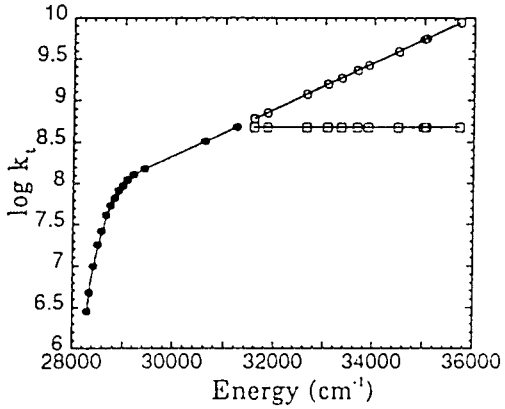

Figure 9. Triplet rate constant as a function of energy. The solid circles below the singlet threshold at 30116.2 cm^{-1} are the data of ref 32. The solid circles above the singlet threshold are calculated from the total rate constant[31] and the singlet yield. The open circles and open squares are the approximated upper and lower limit triplet rate constants described in the text.

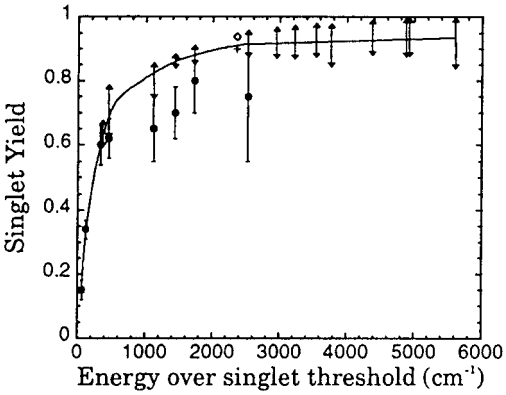

Figure 10. Singlet yield as a function of excess energy. The upper and lower limits calculated here are given by the triangles at either end of the error bars. The solid line is a smooth interpolation given to guide the eye. The solid circles are the earlier estimates of Kim *et al.*[14] The "plus" is the lower limit at 308 nm determined by Hayden *et al.*[20] The diamond is the value measured from the correlated-product-state distributions at 308 nm by Wodtke and co-workers.[19]

$$k_t(E) = (1 - \phi_s(E))k_{tot.}(E) \tag{15}$$

where $\phi_s(E)$ is the singlet yield at that energy. The two triplet rate constants closest in energy below the singlet threshold and the first two above were least-squares fit to a linear log k_t vs E function. Since the slope of the data actually decreases as energy increases, the linear extrapolation overestimates the true rate constants and underestimates the singlet yield. The extrapolated triplet rate constants are shown in Figure 9.

The singlet yield is shown in Figure 10 and compared to that calculated by Kim *et al.*[14] The upper and lower limits are given in Table 2. The singlet yield rises more quickly, and to a higher value than previously predicted. The upper limit of the current and previous results is supported by the more direct determination of 0.94 ± 0.02 for 308 nm photolysis obtained by Wodtke and co-workers.[19] The singlet yields will be used in a later publication to determine the singlet rate constant.[24]

Acknowledgment. This work was supported by the Chemical Sciences Division of the U. S. Department of Energy under Contract No. DE-AC03-76SF00098. A.M. would also like to thank the Deutsche Forschungsgemeinschaft for support. The authors would like to thank Stephen Klippenstein for many

helpful discussions and for providing early access to new var. RRKM rate constants and Douglas Wade for programming assistance.

References and Notes

(1) Gilbert, R. G.; Smith, S. C. *Theory of Unimolecular and Recombination Reactions*; Blackwell Scientific: Oxford, U.K., 1990.
(2) Reisler, H.; Wittig, C. *Annu. Rev. Phys. Chem.* **1986**, *37*, 307.
(3) (a) Green, W. H.; Moore, C. B.; Polik, W. F. *Annu. Rev. Phys. Chem.* **1992**, *43*, 59. (b) Moore, C. B.; Smith, I. W. M. *J. Phys. Chem*., in press.
(4) Baer, T.; Hase, W. L. *Unimolecular Reaction Dynamics: Theory and Experiments*, Oxford University Press: Oxford, U.K., 1996.
(5) (a) Pechukas, P.; Light, J. C. *J. Chem. Phys.* **1965**, *42*, 3281. (b) Pechukas, P.; Rankin, C.; Light, J. C. *J. Chem. Phys.* **1965**, *44*, 794.
(6) Quack, M.; Troe, J. *Ber. Bunsen-Ges. Phys. Chem*. **1974**, *78*, 240.
(7) (a) Quack, M.; Troe, J. *Ber. Bunsen-Ges. Phys. Chem*. **1975**, *79*, 170. (b) Quack, M.; Troe, J. *Ber. Bunsen-Ges. Phys. Chem*. **1975**, *79*, 469.
(8) (a) Troe, J. *J. Chem. Phys.* **1981**, *75*, 226. (b) Troe, J. *J. Chem. Phys.* **1983**, *79*, 6017.
(9) Wittig, C.; Nadler, I.; Reisler, H.; Catanzarite, J.; Radhakrishnan, G. *J. Chem. Phys*. **1985**, *83*, 5581.
(10) (a) Marcus, R. A. *J. Chem. Phys*. **1986**, *85*, 5035. (b) Marcus, R. A. *Chem. Phys. Lett*. **1988**, *144*, 208. (c) Wardlaw, D. M.; Marcus, R. A. *Adv. Chem. Phys.* **1988**, *70*, 231.
(11) (a) Klippenstein, S. J.; Marcus, R. A. *J. Chem. Phys*. **1989**, *91*, 2280. (b) Klippenstein, S. J.; Marcus, R. A. *J. Chem. Phys*. **1990**, *93*, 2418.
(12) Yu, J.; Klippenstein, S. J. *J. Phys. Chem*. **1991**, *95*, 9332.
(13) Nadler, I.; Noble, M.; Reisler, H.; Wittig, C. *J. Chem. Phys.* **1985**, *82*, 2608.
(14) Kim, S. K.; Choi, Y. S.; Pibel, C. D.; Zheng, Q.-K.; Moore, C. B. *J. Chem. Phys*. **1991**, *94*, 1954.
(15) Reid, S. A.; Reisler, H. *J. Phys. Chem.* **1996**, *100*, 474.
(16) Ticich, T. M.; Rizzo, T. R.; Dübal, H.-R.; Crim, F. F. *J. Chem. Phys.* **1986**, *84*, 1508.
(17) Garcia-Moreno, I.; Lovejoy, E. R.; Moore, C. B. *J. Chem. Phys*. **1994**, *100*, 8890.
(18) Garcia-Moreno, I.; Lovejoy, E. R.; Moore, C. B. *J. Chem. Phys*. **1994**, *100*, 8902.
(19) (a) Morgan, C. G.; Drabbels, M.; Wodtke, A. M. *J. Chem. Phys.* **1996**, *104*, 7460. (b) Drabbels, M.; Morgan, C. G.; McGuire, D. S.; Wodtke, A. M. *J. Chem. Phys*. **1995**, *102*, 611.
(20) Hayden, C. C.; Neumark, D. M.; Shobatake, K.; Sparks, R. K.; Lee, Y. T. *J. Chem. Phys*. **1982**, *76*, 3607.
(21) Steffes, B.; Li, X.; Mellinger, A.; Vidal, C. R. *Appl. Phys. B* **1996**, *62*, 87.
(22) Greene, C. H.; Zare, R. N. *J. Chem. Phys*. **1983**, *78*, 6741.
(23) Klippenstein, S. J.; East, A. L. L.; Allen, W. D. *J. Chem. Phys*. **1996**, *105*, 118.
(24) Wade, E. A.; Mellinger, A.; Moore, C. B. *J. Chem. Phys.*, in press.
(25) Chang, B.-C.; Wu, M.; Hall, G. E.; Sears, T. J. *J. Chem. Phys.* **1994**, *101*, 9236.
(26) (a) Green, W. H.; Chen, I.-C.; Moore, C. B. *Ber. Bunsen-Ges. Phys. Chem.* **1988**, *92*, 389. (b) Chen, I. C.; Green, W. H.; Moore, C. B. *J. Chem. Phys.* **1988**, *89*, 314.
(27) Chen, I.-C.; Moore, C. B. *J. Chem. Phys*. **1990**, *94*, 269.
(28) Morse, M. D.; Freed, K. F. *Chem. Phys. Lett*. **1980**, *74*, 49.
(29) Qian, C. X. W.; Ogai, A.; Brandon, J.; Bai, Y. Y.; Reisler, H. *J. Phys. Chem*. **1991**, *95*, 6763.
(30) (a) Neyer, D. W.; Luo, X.; Burak, I.; Houston, P. L. *J. Chem. Phys.* **1995**, *102*, 1645. (b) Neyer, D. W.; Luo, X.; Houston, P. L.; Burak, I. *J. Chem. Phys.* **1993**, *98*, 5095.
(31) Potter, E. D.; Gruebele, M.; Khundkar, L. R.; Zewail, A. H. *Chem. Phys. Lett*. **1989**, *164*, 463.
(32) Chen, I.-C.; Moore, C. B. *J. Chem. Phys*. **1990**, *94*, 263.